
CMS Detector Note

The content of this note is intended for CMS internal use and distribution only

8 August 2007

InterCalibration of the CMS Barrel Electromagnetic Calorimeter Using $\pi^0 \rightarrow \gamma\gamma$ Decays

M. Gataullin, V. Litvin, H. Newman, Y. Yang, R. Y. Zhu

California Institute of Technology, Pasadena, CA 91125, USA

F. Santanastasio, Sh. Rahatlou, D. del Re

Università degli Studi "La Sapienza" and INFN, Sezione di Roma, Rome, Italy

D. Gong, J. Haupt, Y. Kubota, R. Rusack, J. Zhang

School of Physics and Astronomy, The University of Minnesota, MN, USA

J. Branson, E. Dusinger, J. Letts, H. Pi, S. Simon

University of California, San Diego, CA, USA

Abstract

A rapid and precise calibration of the CMS electromagnetic calorimeter must be performed in situ at the LHC in order to fully exploit the physics reach of the CMS experiment. Achieving the design-goal calibration precision of 0.5% will be particularly important for a discovery of the Higgs boson in the two-photon decay channel. In this paper we evaluate the potential of a calibration technique that makes use of photon pairs produced in neutral pion decays, $\pi^0 \rightarrow \gamma\gamma$. At the LHC, such photon pairs will be selected using an online filter farm from the QCD events accepted by the Level-1 triggers. The selection performance is studied with large samples of fully simulated QCD events produced in the entire \hat{p}_\perp range of interest. Assuming a Level-1 trigger rate of 10 kHz, the rate of suitable neutral pion decays is estimated to be about 0.9 kHz. A selection approach suitable for the online farm environment is also investigated and found to give similar π^0 yields.

The π^0 calibration performance is studied using several independent calibration algorithms, which are found to be consistent with each other. Using the selected sample of 300 000 $\pi^0 \rightarrow \gamma\gamma$ candidates, we show that for the majority of the barrel calorimeter, up to $|\eta| < 1.4$, a calibration precision of at least 1% (0.5%) can be attained after as few as 30 (130) hours of data-taking in the low-luminosity scenario of LHC, $\mathcal{L} = 2 \cdot 10^{33} \text{ cm}^{-2} \text{ s}^{-1}$.

1 Introduction

The CMS barrel electromagnetic calorimeter (ECAL) will consist of 61 200 lead tungstate crystals arranged in 170 η -rings of 360 crystals each. The ECAL energy resolution has been recently determined in test beams to be [1]

$$\frac{\sigma(E)}{E} = \frac{2.9\%}{\sqrt{E(\text{GeV})}} \oplus \frac{0.130 \text{ GeV}}{E} \oplus 0.4\%, \quad (1)$$

where the three contributions correspond to the stochastic, noise, and constant terms, respectively. This measurement agrees well with the design-goal performance of a perfectly calibrated detector. For electrons and photons with energies in the range of interest for most physics analyses, $E_{\text{shower}} \sim 100 \text{ GeV}$, the energy resolution will be dominated by the constant term. As a consequence, the performance of the CMS ECAL at the LHC will depend mainly on the quality of its calibration and monitoring. Achieving the design-goal calibration precision of 0.5% will be particularly important for a discovery of the Higgs boson in the decay channel $H \rightarrow \gamma\gamma$, one of the primary goals of the LHC physics program.

Prior to its installation in CMS, the entire barrel ECAL is expected to be pre-calibrated by using cosmic muons [2] and by measuring the crystal-to-crystal variation of the scintillation light yield [3]. These methods are expected to provide a channel-to-channel inter-calibration with a precision of at least 2%. In addition, a significant fraction of ECAL supermodules will be calibrated to a much higher precision using the test beam facility at CERN [1].

For the calibration *in situ* at the LHC, the following calibration strategies have been proposed and studied: 1) ϕ -uniformity inter-calibration with QCD events accepted by the Level-1 jet triggers (“energy-flow” method) is expected to provide a fast inter-calibration with a 1-2% precision [4]; 2) measuring E/p for energetic electrons from $W \rightarrow e\nu$ decays is expected to result in a 0.5% calibration precision for the low pseudorapidity region, $|\eta| < 1.0$, after collecting about 5 fb^{-1} of integrated luminosity [5]; 3) reconstructing the $Z \rightarrow e^+e^-$ decays is expected to provide a ring-to-ring calibration of the η -rings with a precision of about 1% after collecting 2 fb^{-1} of integrated luminosity [6]. In addition, variations in the crystal light output and transmittance will be monitored with a fast laser-based system [7]. A recent review of these calibration methods can be found in Reference [8].

According to the projected LHC performance during the first physics run, these calibration strategies will need several months of data-taking to provide a crystal-to-crystal calibration with a sub-percent precision. Moreover, these calibration methods require a precise knowledge of the tracker material budget as well as a thorough understanding of the tracker performance and alignment. In order to address these issues, it has been recently proposed to calibrate the CMS ECAL with photon pairs produced in neutral pion decays, $\pi^0 \rightarrow \gamma\gamma$. Such photon pairs will be selected using an online filter farm from the QCD events accepted by the Level-1 (L1) triggers. In this paper, we investigate the feasibility of this proposal using large samples of fully simulated QCD events. Only the barrel region, $|\eta| < 1.479$, is currently being considered.

Several collider experiments, most notably Crystal Barrel and HERA-B, have successfully used the $\pi^0 \rightarrow \gamma\gamma$ decays for the calibration of their electromagnetic calorimeters. The Crystal Barrel experiment at LEAR was able to reach a calibration precision of 0.5% using a sample of about 1000 π^0 's per crystal [9]. The HERA-B experiment used a dedicated data stream to collect large samples of π^0 decays from events accepted by the L1 triggers [10]. The HERA-B example is of interest because it demonstrates an ability to overcome challenges similar to those facing the development of fast data analysis and transfer tools on the CMS online filter farm. It should also be noted that a similar calibration strategy is currently being considered for the LHCb experiment [11].

This note is organized as follows: The data sets used for this study are described in Section 2. Section 3 describes the selection of $\pi^0 \rightarrow \gamma\gamma$ decays by using all photon candidates reconstructed in the barrel calorimeter. Section 4 discusses an alternative π^0 selection strategy based on information from regions near the L1 trigger electromagnetic objects, which might be more suitable for the online farm environment. The results of the calibration exercise are given in Section 5. We summarize and conclude in Section 6.

2 Data Sets

Our main data set consists of four million $pp \rightarrow \text{jets}$ QCD events generated with full detector simulation. ORCA version 8.7.3 was used for the event digitization and reconstruction. The low-luminosity scenario of $\mathcal{L} = 2 \cdot 10^{33} \text{ cm}^{-2} \text{ s}^{-1}$ was assumed during the digitization. To simulate effects from pileup, we used a sample of 500K minimum-bias events assuming an average of five inelastic non-diffractive interactions per bunch crossing [12].

This data set was produced in eight different \hat{p}_\perp bins, covering a range from 15 GeV to 300 GeV. The numbers of produced events, N_{gen} , L1 trigger efficiency, ε_{L1} , and L1 event rates, \mathcal{R}_{L1} , are listed in Table 1. The L1 event rate

Table 1: Total number of generated QCD events, L1 trigger efficiency, and L1 event rate for the main data set used in this study. The total cross section predicted by PYTHIA, σ , is also listed.

\hat{p}_\perp (GeV)	σ (mb)	N_{gen}	ε_{L1} (%)	\mathcal{R}_{L1} (kHz)
15-20	1.45500	664K	0.110 ± 0.004	3.202 ± 0.118
20-30	0.63200	509K	0.229 ± 0.007	2.901 ± 0.085
30-50	0.16290	1 402K	0.996 ± 0.008	3.244 ± 0.027
50-80	0.02156	764K	4.661 ± 0.024	2.010 ± 0.010
80-120	0.00308	298K	12.723 ± 0.061	0.783 ± 0.004
120-170	0.00049	233K	37.303 ± 0.100	0.369 ± 0.001
170-230	0.00010	209K	69.766 ± 0.101	0.141 ± 0.000
230-300	0.00002	71K	93.210 ± 0.095	0.046 ± 0.000
Combined	2.275	4 150K	0.279 ± 0.003	12.70 ± 0.15

in a given \hat{p}_\perp bin is calculated as

$$\mathcal{R}_{L1} = \sigma \cdot \mathcal{L} \cdot \varepsilon_{L1}, \quad (2)$$

where σ denotes the total cross section predicted by PYTHIA. The number of produced events in each bin was chosen to be roughly proportional to the rate of π^0 decays selected from this bin (see Section 3.3).

The dependence of the QCD production cross section and L1 trigger efficiency on \hat{p}_\perp is shown in Figures 1a,b. The corresponding event rate after the L1 trigger acceptance cuts is shown in Figure 1c. The total L1 rate is found to be $\sum \mathcal{R}_{L1} = 12.7 \pm 0.2$ kHz, in agreement with previously reported estimates [13]. The ‘‘generator level’’ rates of useful $\pi^0 \rightarrow \gamma\gamma$ decays in different \hat{p}_\perp bins are derived in Appendix A, with the weighted average of useful π^0 decays per QCD event equal to 0.376 ± 0.006 .

We also use a sample of about 800K fully simulated QCD events. These events are used to study the performance of a different selection approach that employs only information from local regions around the L1 electromagnetic candidates, as described in Section 4. This additional data set covers almost the same \hat{p}_\perp range as our main data set (see Table 2). However, a number of different assumptions were made during event generation and digitization:

- Different PYTHIA models were used for the description of multiple interactions [14]. The main data set was generated assuming a flat probability with an abrupt $p_{\perp min}$ cut-off. This model was also used in the DC04 Data Challenge as well as for the simulation of QCD backgrounds for the $H \rightarrow \gamma\gamma$ studies reported in CMS PTDR Vol. II [12]. The additional data set was produced assuming a varying impact parameter with a double Gaussian matter distribution. This newer model seems to be preferred by recent studies of CDF data [14].
- The additional data set was digitized using ORCA version 8.7.4. As a result, the overall L1 rate for the is found to be lower than for the main data set, mainly due to the differing L1 rates in the first two \hat{p}_\perp bins.
- For both data sets the effects of pileup were taken into account during the digitization step, assuming the low-luminosity scenario of $\mathcal{L} = 2 \cdot 10^{33} \text{ cm}^{-2} \text{ s}^{-1}$. However, the additional data set was digitized using an older model for pileup simulation that was used, *e.g.*, for the DC04 Data Challenge. The main data set was produced with a newer pileup model described in CMS PTDR Vol. II [12].

Table 2: Total number of generated QCD events, L1 trigger efficiency, and L1 event rate for the additional data set used in Section 4. The effective cross section ($\sigma_{L1}^{eff} = \sigma \cdot \varepsilon_{L1}$) is also listed.

\hat{p}_\perp (GeV)	N_{gen}	ε_{L1} (%)	\mathcal{R}_{L1} (kHz)	σ_{L1}^{eff} (mb)
15-20	45K	0.051 ± 0.011	1.53 ± 0.32	$(7.7 \pm 1.6) 10^{-4}$
20-30	90K	0.154 ± 0.013	1.85 ± 0.16	$(9.26 \pm 0.78) 10^{-4}$
30-50	90K	0.985 ± 0.033	2.95 ± 0.01	$(1.47 \pm 0.05) 10^{-3}$
50-80	170K	4.76 ± 0.05	1.90 ± 0.02	$(9.52 \pm 0.10) 10^{-4}$
80-120	240K	12.73 ± 0.07	0.764 ± 0.004	$(3.82 \pm 0.02) 10^{-4}$
120-170	135K	37.1 ± 0.1	0.371 ± 0.001	$(1.86 \pm 0.06) 10^{-4}$

In addition, we produced an sample of about two million QCD events digitized without including pileup. This “no-pileup” sample is used to investigate the effects of pileup on the π^0 yield. The results of these studies are summarized in Appendix B.

3 Selection of π^0 Candidates in the Entire Barrel ECAL

In this section, we describe our selection of $\pi^0 \rightarrow \gamma\gamma$ decays using photon candidates reconstructed in the entire barrel electromagnetic calorimeter. The results of this selection approach will be later used for the calibration exercise in Section 5.

The photon candidates from $\pi^0 \rightarrow \gamma\gamma$ decays are constructed into basic clusters using the “island” clustering algorithm [15]. The cluster energy is computed as a sum of energies deposited in crystals forming the 3×3 matrix centered on the crystal with the highest energy deposit:

$$S_9 \equiv \sum_{3 \times 3} C_i \cdot E_i, \quad (3)$$

where C_i denotes the crystal’s calibration constant and E_i the energy deposited in this crystal. In addition, the cluster energy is multiplied by a constant factor of about 1.12 to compensate for incomplete shower containment in the 3×3 crystal matrix and bring the position of the reconstructed $\pi^0 \rightarrow \gamma\gamma$ peak to 135 MeV. The pseudorapidity and azimuthal angle of a photon candidate are obtained by calculating the weighted averages of the positions of the constituent crystals, where the weight is given by the logarithm of the crystal energy [15].

The selection cuts are then based on a limited number of quantities computed using the crystal-level information from a localized region around the π^0 candidate. To be considered in the combinatorial selection of $\gamma\gamma$ pairs, a cluster is required to have a transverse energy greater than 1 GeV. The shape of its energy deposition must be consistent with that of an electromagnetic shower produced by an unconverted photon. This is ensured by requiring that both the S_4/S_9 and S_9/S_{25} ratios should be above 0.9 (see Figures 2a,b). Here, the quantities S_9 and S_{25} correspond to the energies deposited in the 3×3 and 5×5 crystal matrices centered on the crystal with the highest energy deposit, respectively. The quantity S_4 is the highest value of energies deposited in the four possible combinations of 2×2 crystal matrices containing the most energetic crystal.

Photon pairs are then selected by requiring the reconstructed transverse energy of the pair to be above 3.5 GeV. As shown in Figure 2c, this cut proved to be particularly effective in reducing the background contamination. To further enhance the purity of the selected π^0 sample, the following isolation cut is applied: the sum of transverse energies of all basic clusters (excluding the two forming the π^0 candidate) found within $\Delta R \equiv \sqrt{(\Delta\phi)^2 + (\Delta\eta)^2} < 0.2$ and $\Delta\eta < 0.05$ from the π^0 candidate is required to be less than 60% of the transverse energy of the reconstructed π^0 candidate (see Figure 2d). Only clusters with a transverse energy above 0.1 GeV are included in the sum.

Figure 3a shows that the ΔR separation between the photons in selected pairs ranges from about 0.03 to 0.09. The average energies of the most and least energetic photons in the pair are found to be 5.4 GeV and 2.6 GeV, respectively (see Figure 3b). The distributions of the number of crystals per photon candidate are shown in Figure 3c. For the most energetic photon this distribution has two peaks. We performed a dedicated study of this effect using large samples of single-photon events and found that it was caused by the implementation of the selective readout algorithm [17]. On average, the selected clusters are found to consist of only about eight crystals, with the most energetic crystal containing about 70% of the cluster energy (see Figures 3c,d).

3.1 Reconstruction of the π^0 Peak

The invariant mass of the π^0 candidate is reconstructed as

$$M_{\pi^0} = \sqrt{2E_1 E_2 (1 - \cos \theta_{12})}, \quad (4)$$

where E_1 and E_2 are the energies of the two photons and θ_{12} the angle between them. The mass resolution is then given by

$$\frac{\sigma_M}{M_{\pi^0}} = \frac{1}{2} \left(\frac{\sigma_{E_1}}{E_1} \oplus \frac{\sigma_{E_2}}{E_2} \oplus \frac{\sigma_{\theta_{12}}}{\tan(\theta_{12}/2)} \right). \quad (5)$$

The average distance between the two photon candidates is only about three crystals, as shown in Figure 3a. As a result, 80% of the uncertainty on the π^0 mass is due to the uncertainty on the measurement of θ_{12} with the remaining 60% coming from the uncertainties on the reconstructed photon energies (see Figures 4a,b).

Signal π^0 candidates are identified by matching the η and ϕ coordinates of the both reconstructed photons to those of the photons from “generator-level” π^0 decays, as obtained from the PYTHIA event record. Figure 4c shows that the invariant mass distribution for such photon pairs is approximately Gaussian. The mass distribution for the combined signal and background sample is then fitted to a combination of a Gaussian distribution (peak) and a fourth-order polynomial (background). The π^0 mass resolution is obtained as the width of the fitted Gaussian and is found to be 7.8% (see Figure 4d).

3.2 Effects due to Pileup

We use two independent methods to estimate the rate of neutral pion decays from pileup. The first method consists in comparing the invariant mass distributions for the data sets produced with and without pileup. Since we do not have access to the “generator level” information for minimum-bias events, all $\gamma\gamma$ pairs from pileup are categorized as background. Figure 5 shows that the background-only distribution for the QCD sample generated with pileup exhibits a clear π^0 peak, which is absent for the sample produced without pileup (see Appendix B). The rate of π^0 decays from pileup can then be estimated by fitting the background distribution with a combination of a Gaussian function and a fourth-order polynomial (Figure 5).

However, this method does not allow us to identify the $\gamma\gamma$ pairs from pileup. Because the available sample of minimum-bias events is not sufficiently large (only 500K for the entire 4 000K QCD event sample), such pairs are repeated several times in the selected sample of π^0 candidates. Thus, using such π^0 candidates for calibration studies would introduce a noticeable systematic error. In order to identify the $\gamma\gamma$ pairs produced in pileup, we use another method which consists in searching for pairs of $\gamma\gamma$ pairs that match to each other. This matching is defined by the following requirements:

$$|\phi_\gamma^i - \phi_\gamma^j| < 0.01, \quad |\eta_\gamma^i - \eta_\gamma^j| < 0.01, \quad \frac{|E_\gamma^i - E_\gamma^j|}{E_\gamma^i} < 0.1,$$

where the indexes i and j label the two $\gamma\gamma$ pairs and the matching requirements are applied to both photons from each pair. Photon pairs with more than one matching pair are then regarded as coming from pileup. The invariant mass distribution for the photon pairs coming from pileup is shown in Figure 6. This distribution is clearly dominated by the photon pairs coming from genuine $\pi^0 \rightarrow \gamma\gamma$ decays. The rate of π^0 's from pileup is then estimated by fitting such distributions with a combination of a Gaussian function and a fourth-order polynomial.

The results obtained with the two methods are found to be in good agreement. The number of selected π^0 decays from pileup per one collision (QCD event) is estimated to be on average

$$N_{\pi^0}^{pileup}/collision = 0.57 \pm 0.05\%.$$

As expected, this rate is found to be the constant within errors across the entire \hat{p}_\perp range. Since π^0 decays selected in pileup will also be used for the ECAL calibration at the LHC, we adjust our estimates of the π^0 yield accordingly.

3.3 Selection Results

For each \hat{p}_\perp bin, the π^0 yield is calculated as the ratio of the number of selected signal π^0 decays with $M_{fit} - 3 \cdot \sigma_{fit} < M_{inv} < M_{fit} + 3 \cdot \sigma_{fit}$ to the total number of simulated QCD events, where M_{inv} is the invariant mass of the photon pair and M_{fit} and σ_{fit} are the parameters of the fitted Gaussian function. However, since the calibration performance is dominated by photon pairs near the peak ($M_{inv} \simeq M_{fit}$), we calculate the signal-to-background ratio (S/B) using the signal and background rates from a narrower window of $[M_{fit} - 2\sigma_{fit}, M_{fit} + 2\sigma_{fit}]$.

The obtained π^0 yields and S/B ratios are listed in Table 3 for different \hat{p}_\perp bins. To calculate the rate of accepted π^0 decays in a given \hat{p}_\perp bin, the signal yield is multiplied by the L1 event rate:

$$\mathcal{R}_{\pi^0} = r_{sel} \cdot \mathcal{R}_{L1}, \quad (6)$$

where \mathcal{R}_{L1} is defined by Equation 2 (see also Table 1). The background rates are calculated in a similar way. Figures 7a,b show the obtained π^0 rate and S/B ratio as functions of \hat{p}_\perp . The total rate of accepted π^0 decays and S/B ratio are found to be

$$\mathcal{R}_{\pi^0}^{total} = 0.89 \pm 0.01 \text{ kHz}, \quad \langle S/B \rangle = 2.04 \pm 0.02.$$

Table 3: The π^0 yield, signal-to-background ratio, and rate of selected $\pi^0 \rightarrow \gamma\gamma$ decays. The same quantities obtained using only the events accepted by the L1 triggers are also listed.

\hat{p}_\perp (GeV)	All events			Events accepted by the L1 triggers		
	r_{sel} (%)	S/B	\mathcal{R}_{π^0} (kHz)	r_{sel} (%)	S/B	\mathcal{R}_{π^0} (kHz)
15-20	3.32 ± 0.02	2.86 ± 0.04	0.11	3.99 ± 0.75	3.87 ± 1.45	0.13
20-30	4.97 ± 0.03	2.75 ± 0.03	0.14	4.17 ± 0.61	2.27 ± 0.58	0.12
30-50	7.77 ± 0.02	2.14 ± 0.01	0.25	7.71 ± 0.24	1.89 ± 0.10	0.25
50-80	10.64 ± 0.04	1.78 ± 0.01	0.21	10.26 ± 0.18	1.69 ± 0.05	0.21
80-120	12.12 ± 0.07	1.62 ± 0.01	0.09	12.38 ± 0.19	1.65 ± 0.04	0.10
120-170	13.33 ± 0.08	1.56 ± 0.01	0.05	12.73 ± 0.13	1.56 ± 0.02	0.05
170-230	14.16 ± 0.09	1.56 ± 0.02	0.02	13.51 ± 0.10	1.55 ± 0.02	0.02
230-300	14.43 ± 0.15	1.57 ± 0.03	0.01	13.96 ± 0.16	1.58 ± 0.03	0.01
Combined	6.99 ± 0.05	2.04 ± 0.02	0.89 ± 0.01	6.89 ± 0.25	1.96 ± 0.11	0.87 ± 0.03

The π^0 decays from pileup contribute about $8 \pm 1\%$ to the accepted signal rate. After excluding the pileup contribution, the selected sample is found to contain on average about 1.1 π^0 candidates per QCD event. Thus, events with more than one accepted π^0 decay are quite rare. In addition, Figures 8a,b show that both the signal rate and S/B ratio decrease rapidly with pseudorapidity. Therefore, regions of high pseudorapidity will be substantially more difficult to calibrate.

For the calibration at the LHC, π^0 decays will be selected only from the events accepted by the L1 triggers. Using only the subset of such QCD events, the total accepted π^0 rate and S/B ratio are found to be

$$\mathcal{R}_{\pi^0}^{total}(L1) = 0.87 \pm 0.03 \text{ kHz}, \quad \langle S/B(L1) \rangle = 1.96 \pm 0.11.$$

This π^0 rate can be translated into an average of about 1250 selected π^0 decays per barrel crystal per day of continuous data-taking at the LHC. These values are close to those obtained using the entire data set. The agreement is especially good in higher \hat{p}_\perp bins (see Table 3). Thus, we can assume that the L1 trigger cuts do not significantly alter the performance of our selection.

In order to get some understanding of possible systematic errors on the obtained π^0 rates, we compare the selection results obtained using the main and additional data sets. The main sources of systematic uncertainty are found to be due to variations in the Level-1 trigger thresholds and different models used for the simulation of multiple interactions. The total systematic uncertainty on the accepted π^0 rate is found to be about 20%.

Finally, the above results have been obtained assuming a perfectly calibrated ECAL. To estimate the effects of initial miscalibration, we reproduced the same QCD data set with a 4% Gaussian smearing applied to crystal calibration constants (see Equation 3). We find that such initial miscalibration has no noticeable effect on the rate of accepted π^0 decays. However, the S/B ratio decreases by about $6 \pm 2\%$, which is consistent with the broadening of the π^0 mass peak.

4 Selection of π^0 Decays Around L1 Trigger Candidates

The timing constraints of the online farm environment might not allow us to reconstruct all photon candidates in the entire barrel ECAL. In this section, we describe a different selection strategy that uses the L1 trigger electromagnetic candidates to identify regions of interest for a quick selection and reconstruction of π^0 decays. This study is performed using the additional sample of 800K fully simulated QCD events (see Table 2).

4.1 Seeding with L1 Trigger Electromagnetic Candidates

The decisions of the L1 electron and photon triggers are based on input from the Regional Calorimeter Trigger (RCT) [16]. The L1 electromagnetic candidates are found with a sliding window algorithm using the energies deposited in the ECAL trigger towers. Each ECAL trigger tower is formed by a matrix of 5×5 crystals. The L1 electromagnetic candidates are then defined as regions of 4×4 trigger towers, giving a total of 20×20 crystals. As illustrated in Figure 9, each such candidate has fixed $\Delta\eta \times \Delta\phi$ dimensions in the ECAL geometry.

The top four L1 electromagnetic candidates of both the isolated and non-isolated types are forwarded to the Global Calorimeter Trigger. Such candidates can then be used to search for π^0 candidates in the limited regions of ECAL, which would significantly reduce the processing time on the online filter farm.

4.2 Selection Criteria

Within each 20x20 crystal region, photons candidates are reconstructed using a simple clustering algorithm. The algorithm starts by searching for cluster seeds, defined as crystals with a measured energy of at least 0.5 GeV. The seeds are then sorted according to their energy. Starting from the seed with highest energy, a 3x3 cluster centered around the seed is formed, excluding the crystals with non-positive energy. Each crystal is required to belong to only one cluster. Clusters consisting of only one crystal are discarded.

Figures 10 and 11 show typical L1 electromagnetic candidates (containing a reconstructed π^0 candidate) in absence and in presence of background, respectively. The cluster energy is calculated as the sum of the energies of its crystals. The cluster position is given by the energy-weighted average of the constituent crystal positions [15]. The π^0 candidates are then formed from combinations of the constructed clusters that pass the selection cuts described below.

Photons are expected to produce compact showers with most of the energy deposited in the central crystal. Thus, we require $S_1/S_9 > 0.6$ and $S_9/S_{25} > 0.85$, where S_1 is the fraction of cluster energy in the central crystal and the energy sums S_9 and S_{25} are the same as defined in Section 3. Figures 12 and 13 show the distributions of the S_1/S_9 and S_9/S_{25} variables for the signal and background.

The number of clusters reconstructed in the L1 electromagnetic candidate is required to be less than four (see Figure 15). To further reduce the background contamination we compare the energy of the π^0 candidate, E_π , to the sum of energies of all reconstructed clusters in the L1 electromagnetic candidate, E_{tot} . We find that the purity of the selected sample is increased by applying the following cut $(E_{tot} - E_\pi)/E_{tot} < 0.35$ (see Figure 14).

4.3 Selection Results

Figure 16 shows the distribution of the reconstructed $\gamma\gamma$ invariant mass after all selection cuts were applied. The numbers of signal and background candidates are then determined in the same way as described in Section 3.3. The total rate of accepted π^0 decays and signal-to-background ratio are found to be

$$\mathcal{R}_{\pi^0}^{total} = 0.37 \pm 0.01 \text{ kHz}, \quad \langle S/B \rangle = 1.5 \pm 0.1.$$

These results are comparable to those obtained by selecting π^0 decays using photon candidates reconstructed in the entire barrel ECAL given in Section 3.3. Thus, this selection approach can be effectively used on the online filter farm without a substantial decrease in the reconstruction efficiency and purity.

5 Calibration with $\pi^0 \rightarrow \gamma\gamma$ Decays

In this Section, we describe the results of the exercise that we performed to study the potential of the CMS ECAL calibration with $\pi^0 \rightarrow \gamma\gamma$ decays.

5.1 The M_{fit} Calibration Algorithm

To investigate the potential of the $\pi^0 \rightarrow \gamma\gamma$ calibration, we use several independent calibration algorithms, one of which is described below. As discussed in Appendix C, using other algorithms results in a similar calibration performance.

The M_{fit} algorithm uses the invariant mass distributions collected for each individual crystal. For a given crystal, the corresponding histogram is filled with the invariant masses of all π^0 candidates for which one of the photons is centered on this crystal. The obtained histograms are fitted to a fourth-order polynomial for the background and a Gaussian for the π^0 peak, as shown in Figure 4d. The calibration constants are then calculated as

$$C_N(n_\eta, n_\phi) = C_{N-1}(n_\eta, n_\phi) \times \left(\frac{M_{\pi^0}}{M_{fit}} \right)^2, \quad (7)$$

where

- N is the number of the iteration step.
- $C(n_\eta, n_\phi)$ is the calibration constant of a crystal with integer coordinates n_η and n_ϕ in the global ECAL crystal matrix.
- M_{fit} is the fitted peak position.
- M_{π^0} is the nominal value of the π^0 mass.

The fitted π^0 mass for a given crystal is largely unaffected by the errors on the calibration constants of other crystals since these are averaged out and only contribute to the width of the peak. Thus, the new calibration constants should shift the individual π^0 peaks closer to the nominal value of the π^0 mass. After each calibration step, the energy and direction of flight of each photon are recalculated using the updated calibration constants. The method is then iterated until the calibration constants converge.

The main advantage of this method consists in using a much broader window around the π^0 peak, which improves the estimation of background by using the sidebands of the peak.

5.2 Corrections Depending on η and ϕ

Before proceeding to calibration studies, we need to correct for systematic effects due to gaps between the ECAL modules and due to the implementation of selective readout. Figure 17 shows that the reconstructed π^0 mass clearly depends both on the η and ϕ rings numbers. The largest shifts of about -1.5% are due to the gaps between the ECAL supermodules (ϕ -rings) and baskets (η -rings). In addition, a smaller shift of about -0.4% is due to the selective readout algorithm. This shift occurs with a period of five crystals in both the ϕ and η directions, which corresponds to the size of the ECAL trigger towers [17].

To take these effects into account, we perform ring-to-ring calibrations: first for the ϕ crystal rings and then for the η -rings. The obtained calibration constants are then systematically applied as corrections to the energies reconstructed in individual crystals. The cluster energy is still computed as the sum of energies deposited in the 3×3 crystal matrix, but Equation 3 becomes

$$S_9 = \sum_{3 \times 3} D_\eta(n_\eta) \cdot D_\phi(n_\phi) \cdot C_i(n_\eta, n_\phi) \cdot E_i, \quad (8)$$

where $D_\eta(n_\eta)$ and $D_\phi(n_\phi)$ are the correction factors derived from the ring-to-ring calibrations and $C_i(n_\eta, n_\phi)$ is the calibration constant for a crystal whose coordinates are given by two the integer numbers n_η and n_ϕ . This definition of S_9 ensures that the calibration constants still refer to the energies deposited in individual crystals. Further η, ϕ -dependent corrections will have to be derived for higher-level reconstruction algorithms, where the $\{D_\eta(n_\eta)\}$ and $\{D_\phi(n_\phi)\}$ corrections might also prove to be useful. This approach was successfully used for the particle reconstruction with the L3 electromagnetic calorimeter [19].

To verify the validity of this approach, we use half of our selected π^0 sample to derive the correction coefficients and the remaining half to obtain the fitted π^0 mass values. Figures 17a,b show that this procedure eliminates the systematic variations observed as functions of η and ϕ rings numbers.

Because of the limited size of our main Monte Carlo sample, for the calibration studies we use the coefficients obtained using a dedicated sample of about two million QCD events enriched with $\eta \rightarrow \gamma\gamma$ decays. This sample was produced for our previous studies of the potential for a calibration with photons from η meson decays [18].

5.3 Performance of the $\pi^0 \rightarrow \gamma\gamma$ Calibration

For the tests of our calibration algorithms, we use all photon pairs selected from our main data set (see Table 1). To achieve the necessary level of statistical precision, we fold the entire barrel onto a 10×10 crystal matrix. This is done by assuming that the calibration constants are periodic:

$$C_N(n_\eta, n_\phi) = C_N(n_\eta + 10m, n_\phi + 10n), \quad (9)$$

where m and n are integers. The effects of the folding procedure have been investigated by varying the size of folding matrix. As described in Appendix C, no significant systematic bias is observed.

After removing the $\gamma\gamma$ pairs from pileup, the selected sample consists of about 300K signal π^0 decays with a S/B ratio of 1.9. Therefore, the maximum available number of π^0 decays per crystal is on average 3000.

Unless otherwise stated, the calibration tests described in this section are performed with an initial miscalibration of 4% (Gaussian smearing). For a perfectly calibrated crystal, the product of the calibration constant and initial miscalibration factor should be equal to one. The calibration precision is then estimated as the RMS width of the distribution of such products for the 100 calibration constants that remain after the folding onto a 10×10 crystal matrix.

For the signal-only sample, the M_{fit} algorithm gives a calibration precision of $0.45 \pm 0.03\%$ and requires six iterations to converge. For the case of $S/B = 1.9$ the M_{fit} algorithm gives a precision of $0.50 \pm 0.04\%$ and converges after seven iterations. Moreover, the M_{fit} algorithm is found to always converge after six-seven iterations for signal-to-background ratios as low as $S/B = 0.8$.

Applying the η, ϕ -dependent corrections derived in Section 5.2, we find that the calibration precision improves from about 1.2% to 0.5% (see Figure 18). A thorough understanding of the effects due the gaps between the ECAL supermodules/baskets and selective readout will be crucial for the actual calibration at the LHC. As described in Section 5.2, we used a sample of QCD events enriched with $\eta \rightarrow \gamma\gamma$ decays to derive our η, ϕ -dependent corrections. To verify that it will be possible to obtain such corrections using π^0 decays collected at the LHC, we split our selected signal+background sample into two equal subsamples. We use the first subsample to derive a set of the correction factors $\{D_\eta(n_\eta)\}$ and $\{D_\phi(n_\phi)\}$ (see Equation 8). We then find that the calibration precision obtained with the second subsample is about 0.85%. This is only slightly worse than the calibration precision of 0.75% obtained with the correction factors derived using the much larger sample of $\eta \rightarrow \gamma\gamma$ decays.

In order to investigate the dependence of the calibration precision on the number of collected π^0 decays, we split our calibration sample into several subsamples of varying size. As shown in Figure 19, this dependence can be described by the following function:

$$\frac{\sigma_C}{C} = \frac{a}{\sqrt{n_{\pi^0}}} \oplus b, \quad (10)$$

where a and b are constant parameters and n_{π^0} denotes the average number of signal π^0 decays per crystal. The fits are performed for two cases: signal-only and $S/B = 1.9$, which corresponds to the observed background contamination (see Table 3).

If we use the entire calibration sample for each value of n_{π^0} , we obtain the following results: $a = 22.5 \pm 0.4\%$ and $b = 0.12 \pm 0.09\%$ for the signal-only samples; $a = 27.3 \pm 0.5\%$ and $b = 0.17 \pm 0.11\%$ for $S/B = 1.9$. However, this method underestimates the statistical errors on the fitted constants because the errors on the individual data points in Figure 19a are strongly correlated. To avoid this bias, we split our calibration sample into five independent subsamples with about 200 (two samples), 400, 700, and 1500 π^0 's/crystal. These fits produce the following results:

$$\begin{aligned} \frac{\sigma_C}{C}(\text{signal only}) &= \frac{(22.2 \pm 1.1) \%}{\sqrt{n_{\pi^0}}} \oplus (0.18 \pm 0.17) \% , \\ \frac{\sigma_C}{C}(S/B = 1.9) &= \frac{(27.3 \pm 1.2) \%}{\sqrt{n_{\pi^0}}} \oplus (0.20 \pm 0.26) \% . \end{aligned} \quad (11)$$

The corresponding fitted curves are shown in Figure 19b.

For the case of no background, the best possible value of the ‘‘stochastic’’ constant a can be expressed as [20]

$$a_{ideal} = \frac{\sqrt{2} \sigma_M / M_{\pi^0}}{\sqrt{\langle \sum w_k^2 \rangle}}, \quad (12)$$

where σ_M / M_{π^0} is the effective π^0 peak width, w_k is the fraction of cluster energy deposited in the k th crystal of the cluster, and the summation is performed over all constituent crystals. For our calibration sample $\sigma_M / M_{\pi^0} \simeq 10\%$ and $\sqrt{\langle \sum w_k^2 \rangle} \simeq 75\%$, giving $a_{ideal} \simeq 19\%$. Our observed value $a = 22.2 \pm 1.1\%$ agrees with this theoretical limit.

To study the impact of the background contamination, we vary the S/B ratio of our calibration samples. Adding background is expected to change the ‘‘stochastic’’ constant a as

$$a = a_0 \times \sqrt{\frac{S+B}{S}}, \quad (13)$$

where a_0 corresponds to the value for the signal-only case. Figure 20 shows that this parametrization agrees well with the observed dependence.

The above results have been obtained with the assumption of a 4% initial miscalibration. Nevertheless, we find that for a miscalibration in the range of 0 – 10% the final calibration precision is largely the same (see Figure 21).

Using the π^0 rates and S/B ratios from Figure 8, we can translate the results of our studies of the π^0 calibration performance into the time needed to achieve a given level of calibration precision for different η -regions of ECAL. Here, we assume that the total accepted π^0 rate and S/B ratio are equal to those obtained with the subset of events accepted by the L1 triggers (see Section 3.3). Figure 22 shows that the majority of the barrel calorimeter, up to $|\eta| < 1.4$, can be calibrated to a 1% precision after about 30 hours of data-taking at the LHC. The time required to achieve a 0.5% precision is found to range from about 40 hours for $|\eta| \simeq 0$ to 130 hours for $|\eta| \simeq 1.4$.

6 Conclusions

We study the potential of the calibration of the CMS barrel electromagnetic calorimeter with photons from $\pi^0 \rightarrow \gamma\gamma$ decays. Using large samples of fully simulated QCD events, we have developed a selection of π^0 candidates from QCD events accepted by the Level-1 triggers. The selection is based solely on the crystal-level information from local regions around the π^0 candidates. The rate of accepted π^0 decays is estimated to be about 1250 π^0 's/crystal per day of data-taking at the LHC ($\mathcal{L} = 2 \cdot 10^{33} \text{ cm}^{-2} \text{ s}^{-1}$), with a signal-to-background ratio of about two. We also investigate an alternative selection strategy that uses the L1 trigger input to identify regions of interest for a quick selection and reconstruction of π^0 decays. This selection approach results in a similar π^0 yield so that it can be effectively used on the online filter farm.

Several independent calibration algorithms have been developed and proved to give consistent results. Using our selection results, we show the π^0 calibration method can potentially allow us to calibration the majority of the barrel calorimeter, up to $|\eta| < 1.4$, to at least a 1% (0.5%) precision after about 30 (130) hours of data-taking in the low-luminosity scenario of LHC.

The π^0 calibration will also provide an excellent tool for monitoring of short-term variations in the response of small regions of ECAL. For instance, it can be used to study hourly variations in the response of η -rings with a 1% precision. However, the π^0 calibration is unlikely to eliminate the need for a fast laser-based monitoring system [7].

It should be noted that the π^0 calibration method uses photons with energies about an order of magnitude lower than those of the photons expected to be produced in Higgs decays. Recent results from low-energy electron test beams at H2 indicate that the ECAL response is linear to within a few percent over this range of electron energies [21]. A calibration study has recently been carried out using π^0 decays produced in π^- test beam runs performed in November 2006 [22]. This study confirmed that the CMS ECAL is capable of reconstructing the low-energy photons produced in $\pi^0 \rightarrow \gamma\gamma$ decays and showed that the calibration constants obtained using π^0 decays could be successfully used for the reconstruction of 50 GeV electrons.

More precise measurements of the ECAL non-linearity will have to be performed *in situ* at the LHC in order to validate the π^0 calibration for higher energy scales. This task can be accomplished by calibration studies with electrons from $W \rightarrow e\nu$ [5] and $Z \rightarrow e^+e^-$ decays [6].

Appendix A $\pi^0 \rightarrow \gamma\gamma$ Decays at the Generator Level

It is worthwhile to investigate the rate of useful $\pi^0 \rightarrow \gamma\gamma$ decays at the “generator level,” *i.e.*, using information from the PYTHIA event record. Such decays are selected by requiring the π^0 transverse momentum to be above 3.5 GeV and $\eta - \phi$ separation between the produced photons to be $\Delta R \equiv \sqrt{(\Delta\phi)^2 + (\Delta\eta)^2} > 0.03$. In addition, both photons in the pair should have a transverse momentum above 1 GeV and be in the barrel fiducial region, $|\eta| < 1.479$. This set of cuts corresponds to the phase-space of our $\pi^0 \rightarrow \gamma\gamma$ selection (see the next section).

Figure 23a shows that the number of such π^0 decays per QCD event increases from 0.09 for the bin $\hat{p}_\perp = 15 - 20$ GeV to about 2.1 for the bin $\hat{p}_\perp = 230 - 300$ GeV. The weighted average is calculated by weighting the π^0 rates obtained in different \hat{p}_\perp bins with the corresponding L1 event rates (see Equation 2 and Table 1), giving

$$N_{\pi^0}/event = 0.352 \pm 0.002.$$

It is also interesting to estimate the effects of the L1 trigger acceptance cuts on the π^0 rate. This can be done by using only those QCD events that pass the L1 acceptance cuts. For such QCD events, the weighted average for the number of π^0 decays per QCD event is found to be

$$N_{\pi^0}/event = 0.376 \pm 0.006,$$

which corresponds to a difference of about $+7 \pm 2\%$ with respect to the π^0 rate obtained with the entire QCD data sample (see Figure 23b). Such an increase is expected to occur because the L1 trigger cuts are designed to select events with higher levels of activity in the detector.

Appendix B No-Pileup Data Set

We also produced a sample of about two million QCD events digitized without including pileup. This data set has already been used to study the effects of pileup on the accepted π^0 rate, as described in Section 3.2.

At the LHC start-up, the pileup is expected to be negligible. Therefore, it is interesting to compare the signal yields and background contamination obtained with and without pileup. The results of this comparison are summarized in Table 4. The inclusion of pileup leads to a relative increase of about 5% in the accepted π^0 rate, which is consistent with the estimate derived in Section 3.2. However, the inclusion of pileup also increases the background contamination by about 25%. The observed effect is higher at low values of \hat{p}_\perp . For instance, in the bin $\hat{p}_\perp = 15 - 20$ GeV the inclusion of pileup almost doubles the background contamination.

Table 4: Signal yields and signal-to-background ratios obtained with the Caltech data sets produced with and without pileup. The total number of events generated without pileup, N_{gen} , is also listed. The “no-pileup” combinations are performed using the L1 rates listed in Table 1.

\hat{p}_\perp (GeV)	No pileup			With pileup	
	N_{gen}	$r_{sel}(\%)$	S/B	$r_{sel}(\%)$	S/B
15-20	249K	2.82 ± 0.03	4.73 ± 0.14	3.32 ± 0.02	2.86 ± 0.04
20-30	250K	4.57 ± 0.04	3.36 ± 0.07	4.97 ± 0.03	2.75 ± 0.03
30-50	680K	7.41 ± 0.03	2.32 ± 0.02	7.77 ± 0.02	2.14 ± 0.01
50-80	277K	10.36 ± 0.06	1.82 ± 0.02	10.64 ± 0.04	1.78 ± 0.01
80-120	259K	11.87 ± 0.07	1.66 ± 0.02	12.12 ± 0.07	1.62 ± 0.01
120-170	181K	13.10 ± 0.09	1.64 ± 0.02	13.33 ± 0.08	1.56 ± 0.01
170-230	174K	14.08 ± 0.10	1.61 ± 0.02	14.16 ± 0.09	1.56 ± 0.02
230-300	90K	14.63 ± 0.14	1.63 ± 0.03	14.43 ± 0.15	1.57 ± 0.03
Combined	2159K	6.61 ± 0.05	2.44 ± 0.03	6.99 ± 0.05	2.04 ± 0.02

Appendix C Summary of Other Calibration Algorithms

In this appendix, we provide a brief description of other calibration algorithms that we have developed in addition to the M_{fit} algorithm described and used in Section 5.

The L3 Algorithm.

Iterative algorithms of this type employ the same principle as the algorithm that was developed and used for the calibration of the crystal electromagnetic calorimeter of L3 [19]. One particular implementation of this algorithm is described below.

After each iteration step, the crystal calibration constants are obtained as follows:

$$C_N(n_\eta, n_\phi) = C_{N-1}(n_\eta, n_\phi) \times \frac{1}{\sum_{i=1}^{n_{phot}} w_i} \sum_{i=1}^{n_{phot}} \left(\frac{M_{\pi^0}}{M_{inv}} \right)^2 w_i, \quad (14)$$

where

- N is the number of the iteration step.
- $C(n_\eta, n_\phi)$ is the calibration constant of a crystal with integer coordinates n_η and n_ϕ in the global ECAL crystal matrix.
- n_{phot} is the number of selected photon candidates containing this crystal in the 3×3 crystal matrix.
- w_i is the weight assigned to the i th photon candidate, calculated as the ratio of the energy deposited in this crystal to the total energy deposited in the 3×3 crystal matrix; these energy quantities are computed with calibration constants from the previous iteration step, $\{C_{N-1}\}$.

- M_{inv} is the reconstructed invariant mass of the corresponding $\gamma\gamma$ pair, also computed with $\{C_{N-1}\}$.
- M_{π^0} is the nominal value of the π^0 mass.

For the L3 algorithm, we use only the photon pairs with a reconstructed invariant mass in the range of $[M_{fit} - 2\sigma_{fit}, M_{fit} + 2\sigma_{fit}]$, where M_{fit} and σ_{fit} are the parameters of the fitted Gaussian function (see Section 3.3). After each step, the energy and direction of flight of each photon are recalculated using the updated calibration constants and the π^0 sample used for the calibration is reselected. The iterations are repeated until the calibration constants converge.

It should be noted that a similar algorithm has also been used to study the potential of the ECAL calibration with $Z \rightarrow e^+e^-$ decays [6].

The calibration precisions obtained using the M_{fit} and L3 methods are compared in Figure 24a for the case of $S/B = 1.9$ and in Figure 24b for the signal-only sample (after removing all background). In both cases the same signal sample of 3 000 π^0 's per crystal is used.

For the signal-only sample, the M_{fit} algorithm gives a calibration precision of $0.45 \pm 0.03\%$ and requires six iterations to converge, whereas the L3 algorithm gives the same precision and requires ten iterations to converge. However, for the case of $S/B = 1.9$ the M_{fit} algorithm performs slightly better: it gives a precision of $0.50 \pm 0.04\%$ and converges after seven iterations, whereas the L3 algorithm gives a precision of $0.55 \pm 0.04\%$ and converges after about fifteen iterations. This difference in performance is expected since the M_{fit} algorithm provides a better estimate of background by using the sidebands of the π^0 peak.

The Matrix Inversion Algorithm.

Two calibration algorithms based on the matrix inversion method has been investigated, one of which is described below.

This method solves the linear equations arising from the minimization conditions of χ^2 , given by the variance of the measured π^0 mass from the nominal value. Since the equations are not linear, the final solution is obtained iteratively using a linear approximation. This is equivalent to the Newton's method for finding the root of a set of functions.

The invariant mass squared of a photon pair is given by $4E_{\gamma_1}E_{\gamma_2}\sin^2\theta/2$, where $E_{\gamma_1} = \sum_{i \in \gamma_1} \tilde{E}_i$ ($E_{\gamma_2} = \sum_{j \in \gamma_2} \tilde{E}_j$) is the energy of γ_1 (γ_2) measured in a 3×3 crystal matrix, and θ is the opening angle. \tilde{E}_i is the energy deposited in the i th crystal. If we define the fractional change in the calibration constants to be δ_i , χ^2 is defined as

$$\chi^2 = \left(\frac{4 \sum_{i \in \gamma_1} (\tilde{E}_i + \delta_i \tilde{E}_i) \sum_{j \in \gamma_2} (\tilde{E}_j + \delta_j \tilde{E}_j) \sin^2 \theta / 2 - m_\pi^2}{\sigma_{m^2}^2} \right)^2,$$

where $\sigma_{m^2}^2$ is the resolution of the invariant mass squared.

The energy deposit in the i th crystal estimated after the calibration would then be $\tilde{E}_i + \delta_i \tilde{E}_i$, where \tilde{E}_i is the deposited energy calculated using the initial calibration constant and δ_i is the fractional correction factor to the constants to be determined. By substituting the measured values of the photon energy, the above equation becomes

$$\sum_{i \in \gamma_1} (\tilde{E}_i + \delta_i \tilde{E}_i) \sum_{j \in \gamma_2} (\tilde{E}_j + \delta_j \tilde{E}_j) \sim \frac{m_\pi^2}{\theta^2}.$$

Using \tilde{E}_{γ_1} and \tilde{E}_{γ_2} to represent the measured photon energies, we obtain

$$\tilde{E}_{\gamma_1} \equiv \sum_{i \in \gamma_1} \tilde{E}_i; \quad \tilde{E}_{\gamma_2} \equiv \sum_{j \in \gamma_2} \tilde{E}_j$$

and

$$\Delta W \equiv \frac{m_\pi^2}{\theta^2} - \tilde{E}_{\gamma_1} \tilde{E}_{\gamma_2}.$$

Ignoring terms higher than quadratic in δ , this can be rewritten as

$$\sum_{i \in \gamma_1} \delta_i \tilde{E}_i \tilde{E}_{\gamma_2} + \sum_{j \in \gamma_2} \delta_j \tilde{E}_j \tilde{E}_{\gamma_1} = \Delta W.$$

Defining

$$\tilde{E}_k' \equiv \begin{cases} \tilde{E}_k \tilde{E}_{\gamma_2}, & k \in \gamma_1 \\ \tilde{E}_k \tilde{E}_{\gamma_1}, & k \in \gamma_2, \end{cases}$$

gives us

$$\sum_{k \in \gamma_1, \gamma_2} \delta_k \tilde{E}_k' = \Delta W. \quad (15)$$

Furthermore, we can redefine χ^2 as

$$\chi^2 = \sum_u \left(\frac{\sum_{k \in \gamma_1, \gamma_2} \delta_k \tilde{E}_k' - \Delta W}{\sigma_W} \right)^2,$$

where σ_W is the resolution of the square of the π^0 mass divided by θ^2 . By setting the first derivative to zero

$$\sum_u \left(\frac{\sum_{k \in \gamma_1, \gamma_2} \delta_k \tilde{E}_k' - \Delta W}{\sigma_W^2} \right) \tilde{E}_j' = 0,$$

we obtain

$$\begin{aligned} \sum_{k \in \gamma_1, \gamma_2} \delta_k A_{kj} &= R_j, \\ A_{kj} &\equiv \sum_u \frac{\tilde{E}_k' \tilde{E}_j'}{\sigma_W^2}; \quad R_j \equiv \sum_u \frac{\Delta W}{\sigma_W^2} \tilde{E}_j'. \end{aligned} \quad (16)$$

The calibration constants, δ_k , are then obtained by solving numerically the above system of linear equations, using a matrix inversion algorithm.

Figure 25 shows the calibration precision obtained with the matrix inversion algorithm, as a function of the number of signal π^0 decays per crystal. The obtained results are fitted to the function given by Equation 10. Good agreement with the results given in Section 5.3 is observed. Figure 26 shows that the folding procedure does not lead to a noticeable systematic bias.

References

- [1] P. Adzic *et al.* [CMS ECAL Collaboration], “Results of the first performance tests of the CMS electromagnetic calorimeter,” *Eur. Phys. J. C* **44S2**, 1 (2006).
- [2] F. Ferri and P. Govoni, “The CMS Electromagnetic Calorimeter Pre-calibration with Cosmic Rays and Test Beam Electrons,” **CMS CR-2007/012**; T. Camporesi *et al.*, “Pre-calibration of the CMS ECAL with Cosmic Ray Muons,” **CMS DN-2007/009**.
- [3] F. Cavallari *et al.*, “CMS ECAL intercalibration of ECAL crystals using laboratory measurements,” **CMS NOTE-2006/073**.
- [4] D. I. Futyan, “Intercalibration of the CMS Electromagnetic Calorimeter Using Jet Trigger Events,” **CMS NOTE-2004/007**.
- [5] L. Agostino *et al.*, “Inter-Calibration of the CMS Electromagnetic Calorimeter with Isolated Electrons,” **CMS NOTE-2006/021**.
- [6] P. Meridiani and R. Paramatti, “Use of $Z \rightarrow e^+e^-$ events for ECAL calibration,” **CMS NOTE-2006/039**.
- [7] L. Y. Zhang *et al.*, “Performance of the Monitoring Light Source for the CMS Lead Tungstate Crystal Calorimeter,” *IEEE Trans. Nucl. Sci.* **52**, 1123 (2005).
- [8] G. Daskalakis, “CMS ECAL Calibration Strategy,” **CMS-CR-2006-065**.
- [9] E. Aker *et al.* [Crystal Barrel Collaboration], “The Crystal Barrel spectrometer at LEAR,” *Nucl. Instrum. Meth. A* **321**, 69 (1992).
- [10] B. Giacobbe, “The electromagnetic calorimeter of the HERA-B experiment,” *Nucl. Phys. Proc. Suppl.* **150**, 257 (2006).
- [11] I. Korolko *et al.*, “On the possibility of in situ calibration of LHCb calorimeters,” **LHCb 2000-051**.
- [12] CMS Physics TDR, Volume 2, **CERN-LHCC-2006-001**.
- [13] S. Vanini *et al.*, “2E33 Trigger Tables for PTDR, volume 2,” **CMS AN-2006/085**.
- [14] T. Sjostrand, S. Mrenna, P. Skands, “PYTHIA 6.4 Physics and Manual,” *JHEP* **0605**, Chapter 11, 026 (2006).
- [15] E. Meschi *et al.*, “Electron Reconstruction in the CMS Electromagnetic Calorimeter,” **CMS NOTE-2001/034**.
- [16] The CMS Collaboration, “CMS TDR 6.1 - the TriDAS Project,” **CERN/LHCC 2000-38**.
- [17] S. Rutherford, “Study of the Effects of Data Reduction Algorithms on Physics Reconstruction in the CMS ECAL,” **CMS NOTE-2003/001**.
- [18] V. Litvin, H. Newman, S. Shevchenko, “ECAL Barrel Calibration at LHC Startup with $\eta \rightarrow \gamma\gamma$ Decays,” **CMS IN-2004/021**.
- [19] U. Chaturvedi *et al.*, “Results of L3 BGO Calorimeter Calibration using an RFQ accelerator,” *IEEE Trans. Nucl. Sci.* **47**, 2101 (2000).
- [20] A. Poblaguev, “Comments to the ECAL calibration algorithm,” ECAL-egamma meeting, August 18, 2005.
- [21] D. Gong, Y. Kubota, R. Rusack, J. Zhang, “Analyze the π^0 Runs,” H2 TB06 Analysis meeting, December 21, 2006; N. Pastrone, “Linearity Studies at H2-H4,” ECAL Week, October 25, 2006.
- [22] M. Gataullin *et al.*, “Intercalibration of the CMS Electromagnetic Calorimeter Using $\pi^0 \rightarrow \gamma\gamma$ Decays from 2006 Test Beams,” **CMS DN-2007/007**.

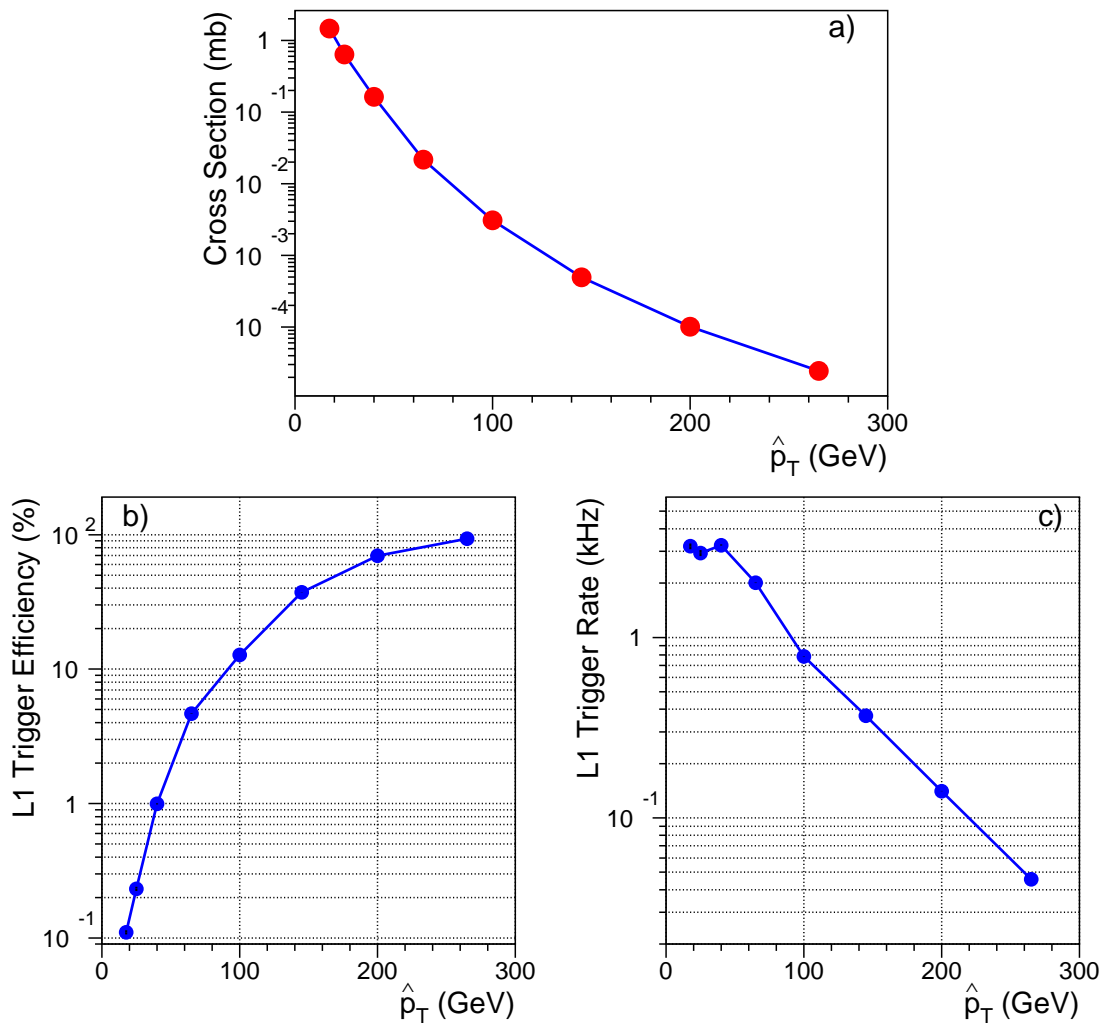


Figure 1: a) Total production cross section, b) L1 trigger efficiency, and c) L1 event rate as functions of \hat{p}_T .

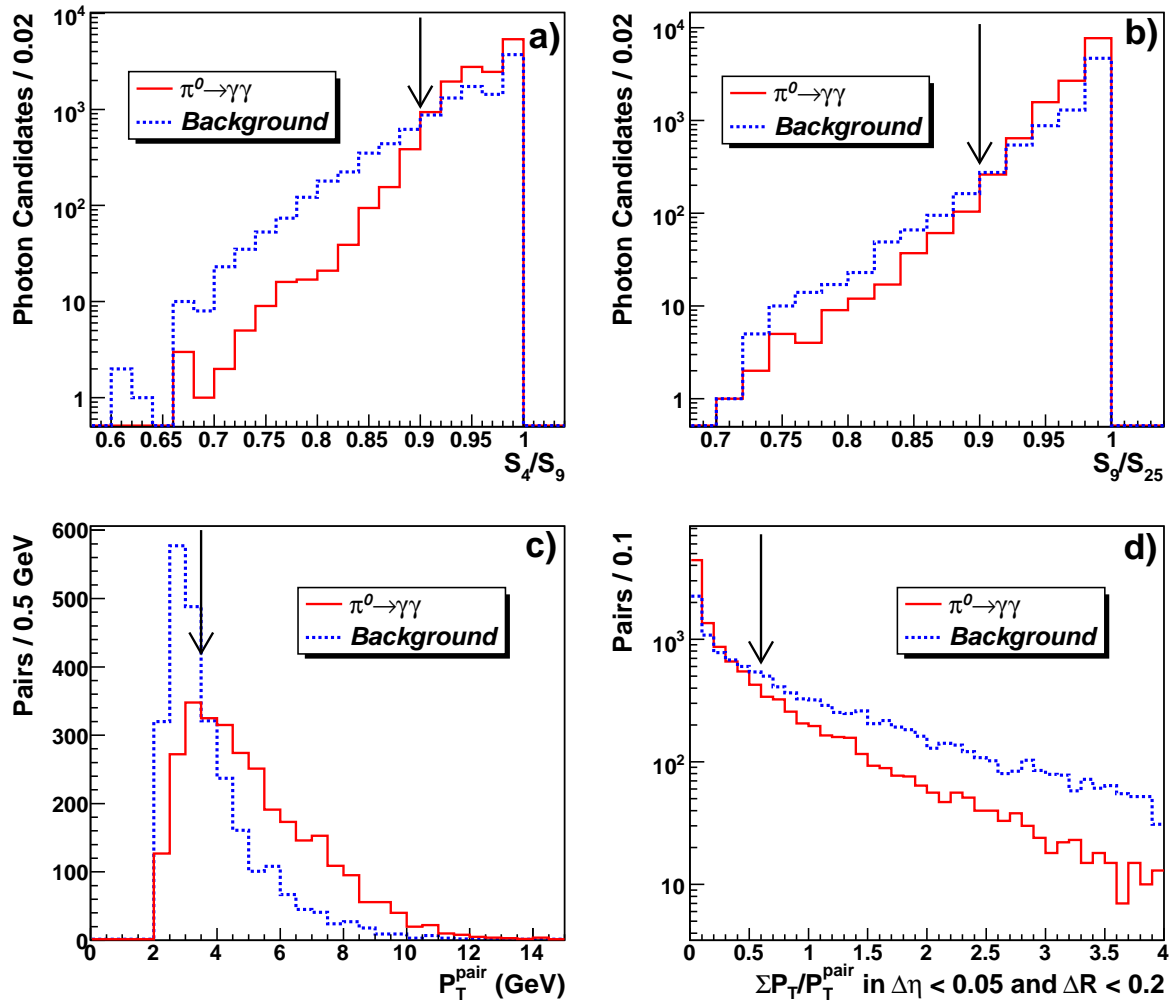


Figure 2: “N-1 cut” distributions for the cuts used in the selection of $\pi^0 \rightarrow \gamma\gamma$ decays. Each distribution is obtained after all other cuts have been applied. The arrows indicate the values of the cuts.

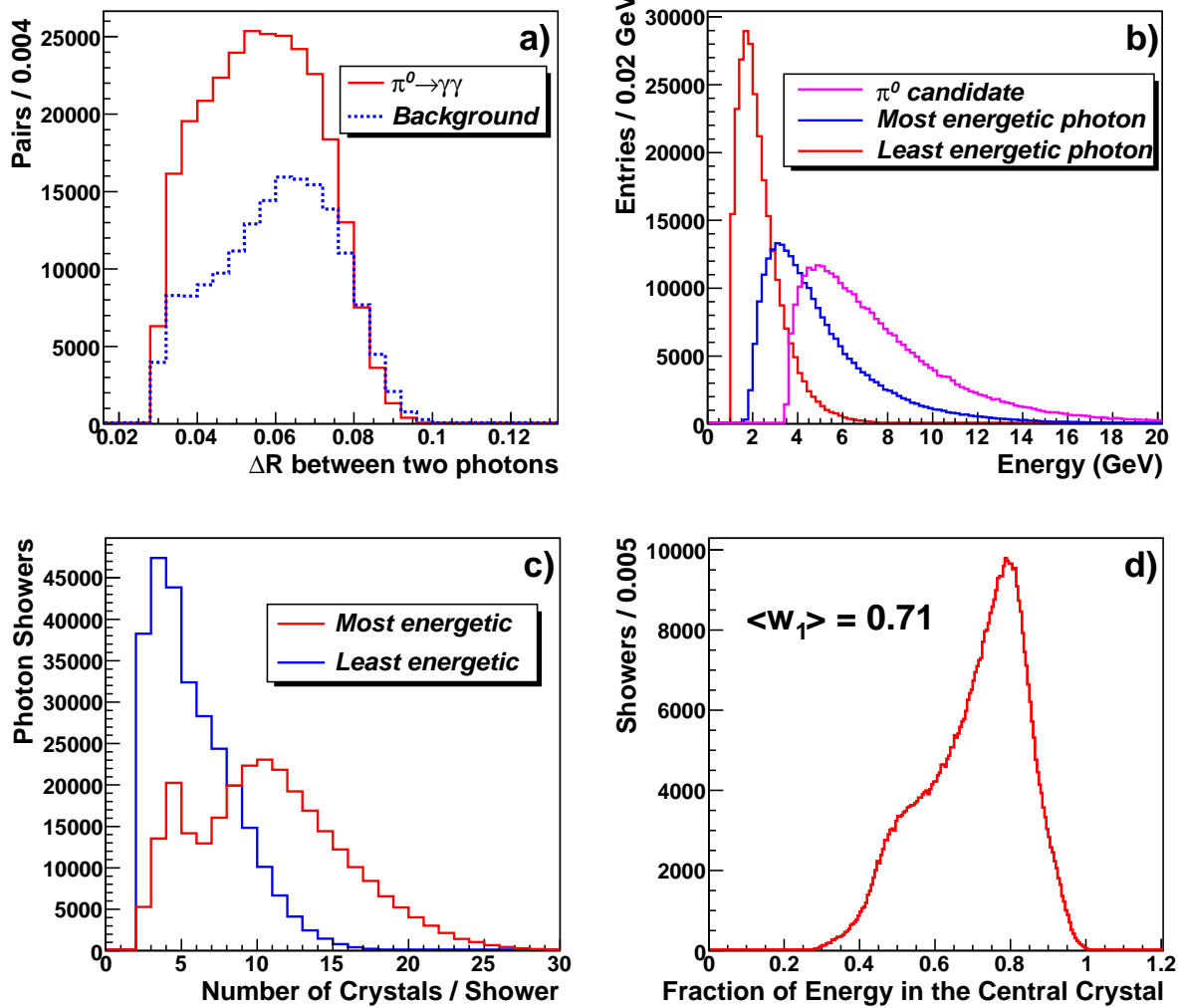


Figure 3: a) Distributions of the ΔR separation between the two photons for the entire selected sample. Distributions of b) the photon and π^0 energies, c) the number of crystals per photon shower, and d) the fraction of the shower energy deposited in the most energetic crystal, for the signal-only sample.

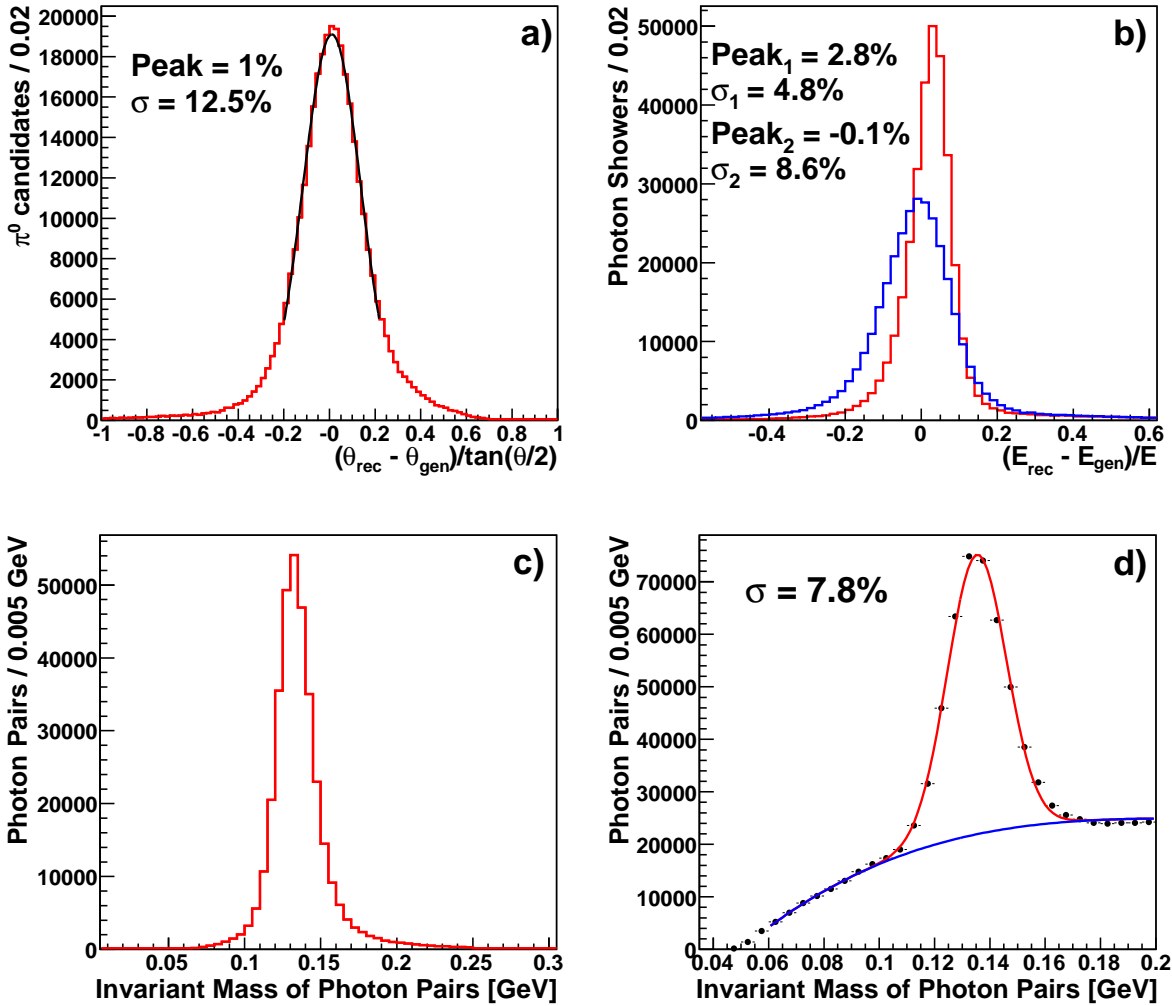


Figure 4: a) Distribution of $(\theta_{rec} - \theta_{gen})/\tan(\theta_{rec}/2)$, where θ denotes the angle between the two photons in a pair, and b) distributions of $(E_{rec} - E_{gen})/E_{rec}$ for the most and least energetic photons in the pair. These distributions are obtained using the photon pairs identified as coming from $\pi^0 \rightarrow \gamma\gamma$ decays (signal-only sample). The $\gamma\gamma$ invariant mass distributions for c) the signal-only and d) signal and background samples. All of the above distributions are obtained using the entire calibration sample digitized with pileup, after applying all selection cuts described in Section 3.

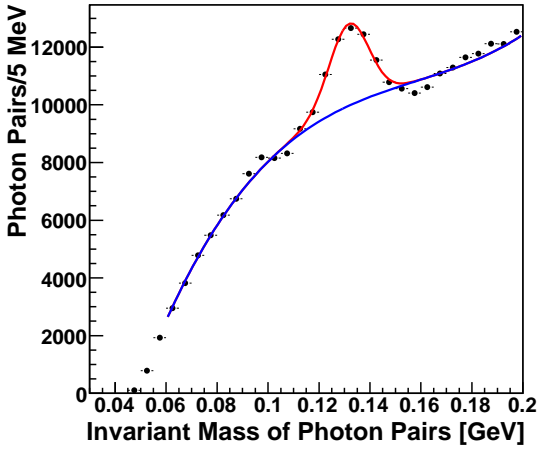


Figure 5: Invariant mass distribution for photon pairs not matching to “generator-level” π^0 decays from the QCD samples simulated with pileup.

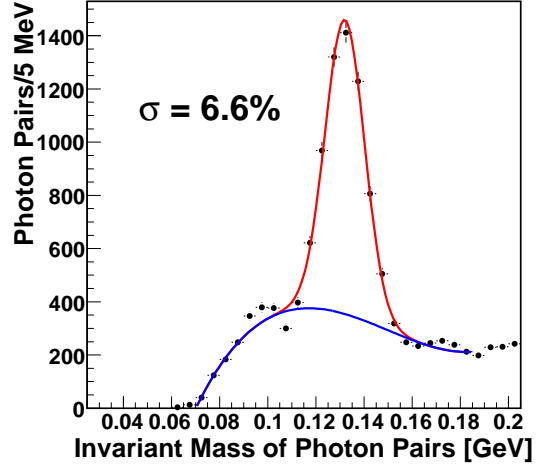


Figure 6: Invariant mass distribution of the photon pairs identified as coming from pileup.

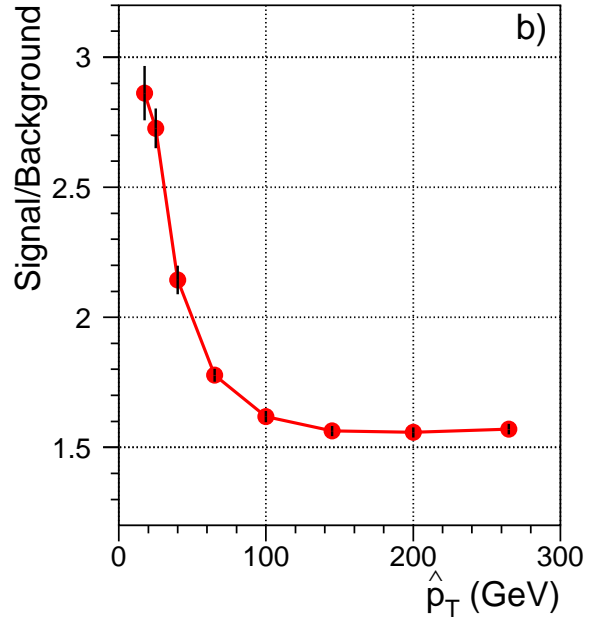
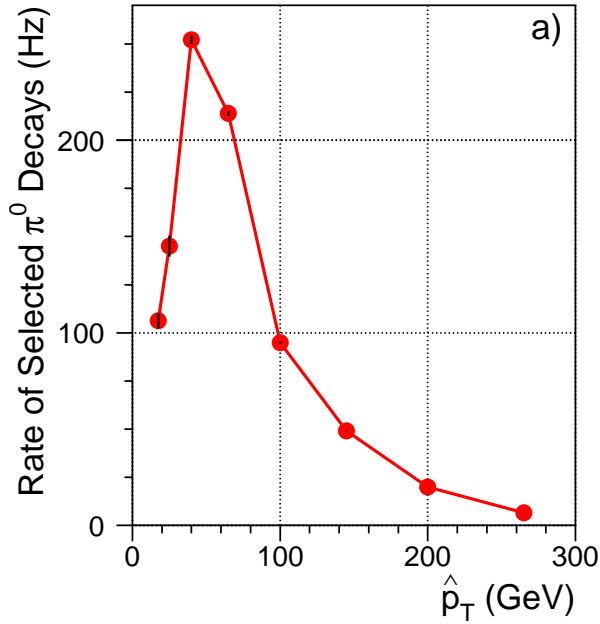


Figure 7: a) Rate of accepted $\pi^0 \rightarrow \gamma\gamma$ decays and b) signal-to-background ratio as functions of \hat{p}_\perp .

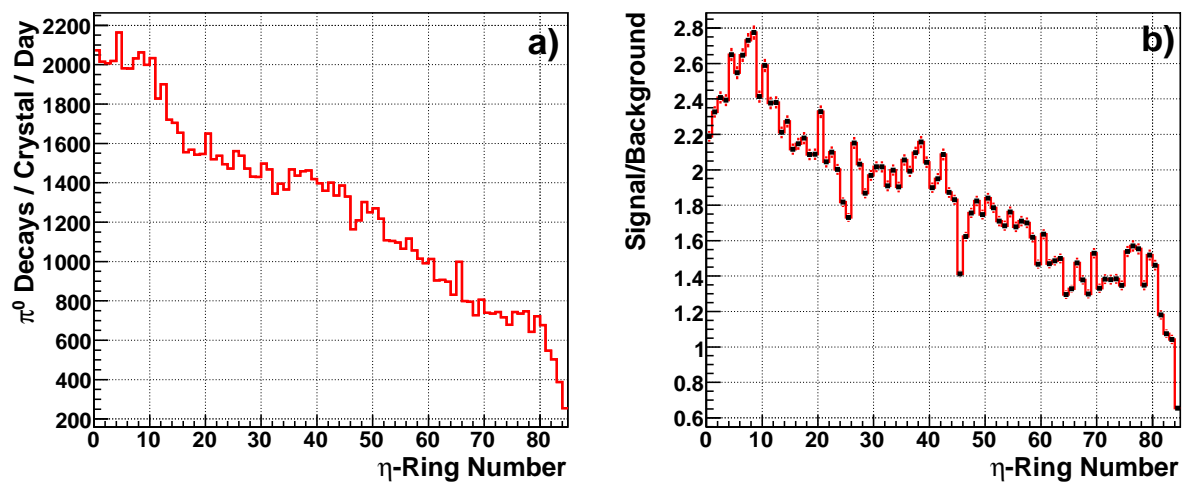


Figure 8: a) Rate of accepted $\pi^0 \rightarrow \gamma\gamma$ decays and b) S/B ratio as functions of the η -ring number.

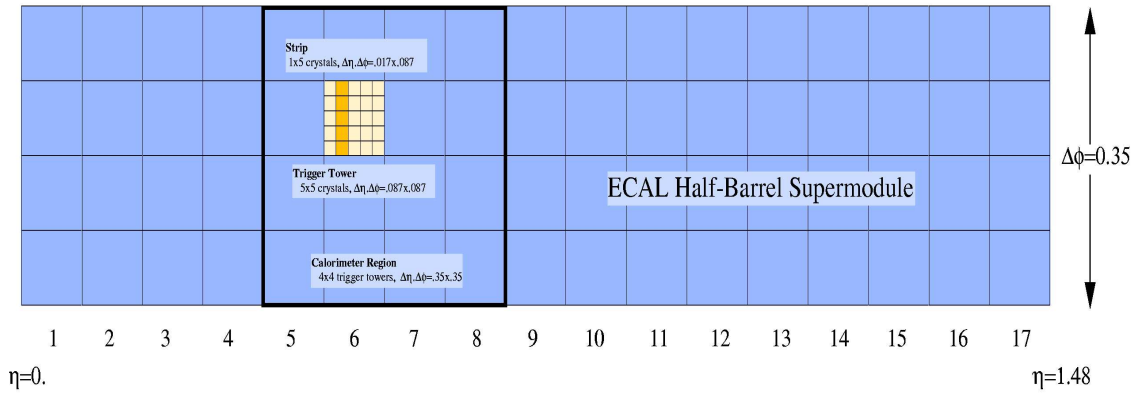


Figure 9: Calorimeter Trigger Tower layout in one ECAL half barrel super module. The trigger towers are organized in calorimeter regions of 4×4 towers.

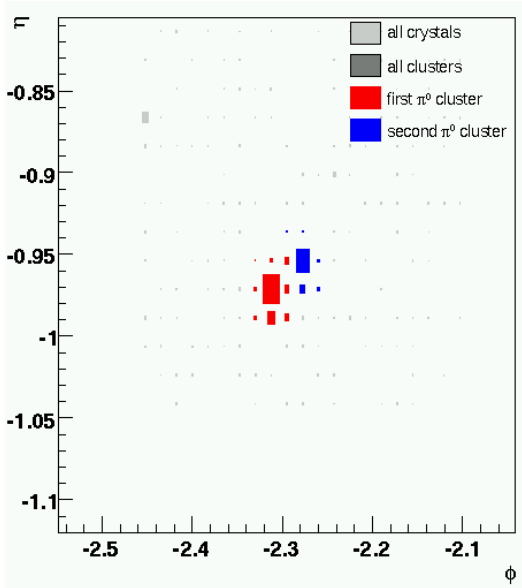


Figure 10: Typical L1 electromagnetic candidate containing a reconstructed π^0 candidate in the absence of noticeable background.

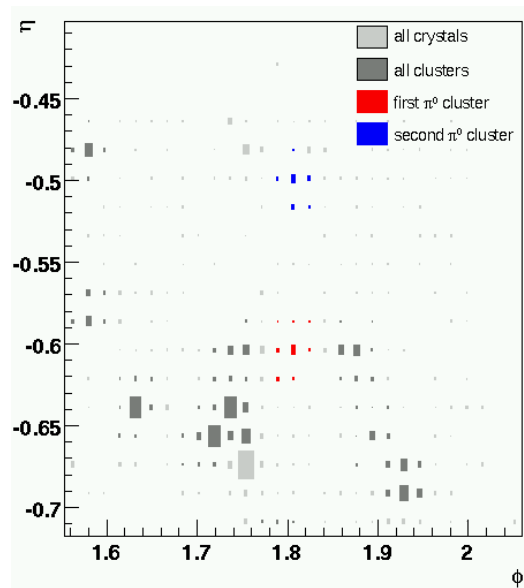


Figure 11: Typical L1 electromagnetic candidate containing a reconstructed π^0 candidate in the presence of background.

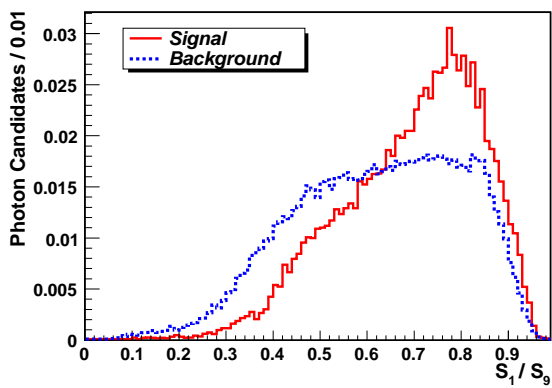


Figure 12: Distribution of S_1/S_9 .

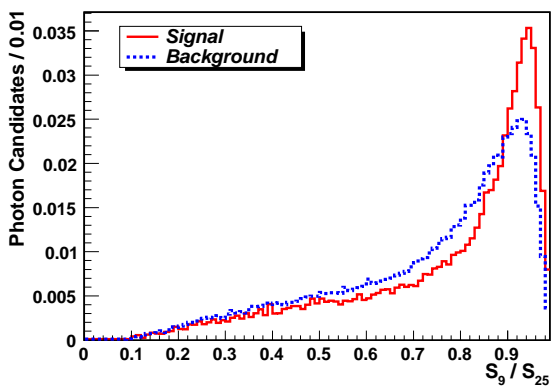


Figure 13: Distribution of S_9/S_{25} .

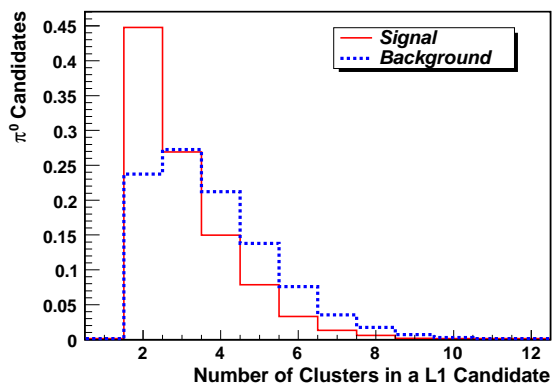


Figure 14: Distribution of the number of clusters reconstructed in a L1 electromagnetic candidate.

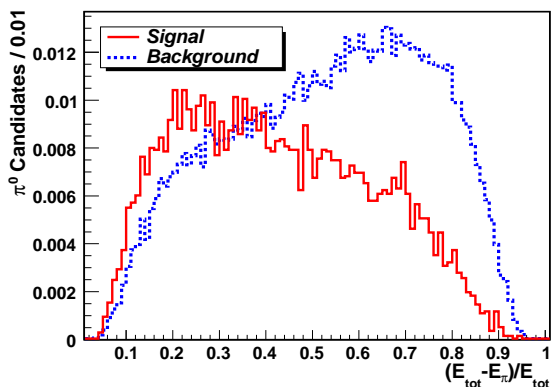


Figure 15: Distribution of the $(E_{tot} - E_{\pi})/E_{tot}$ variable.

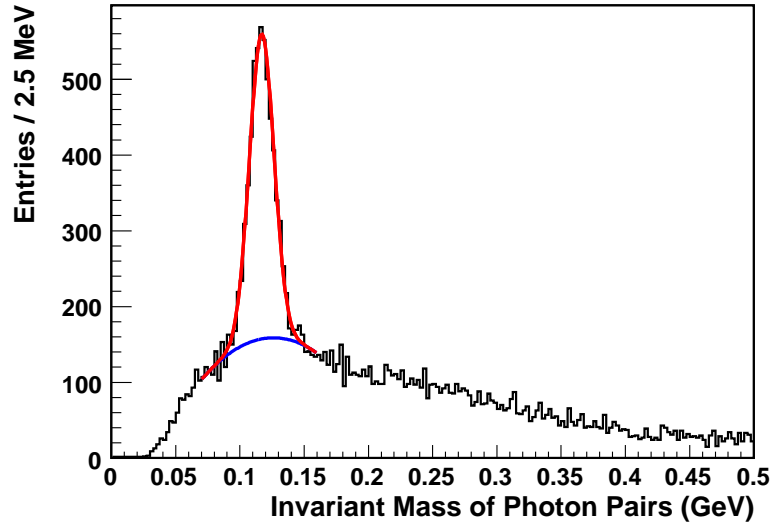


Figure 16: Invariant mass distribution of the photon pairs selected in the regions of interest defined by the L1 trigger electromagnetic candidates. The results of the fit to a combination of a Gaussian distribution and a second-order polynomial are also shown.

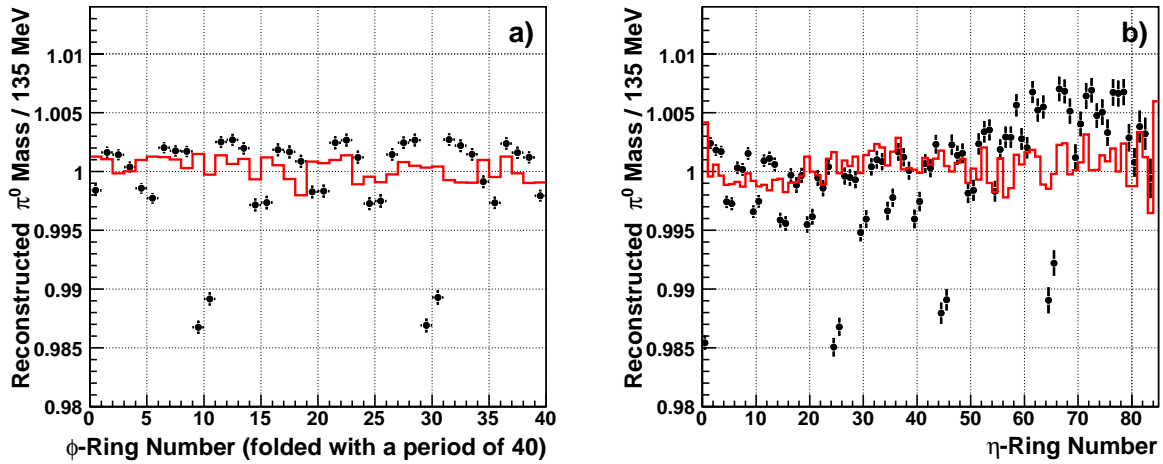


Figure 17: Fitted π^0 -meson masses, normalized to the nominal value of 135 MeV, as functions of a) the ϕ -ring and b) η -ring numbers. The dots represent the values obtained before applying the ring-by-ring corrections, while the histogram shows the improvement after the corrections.

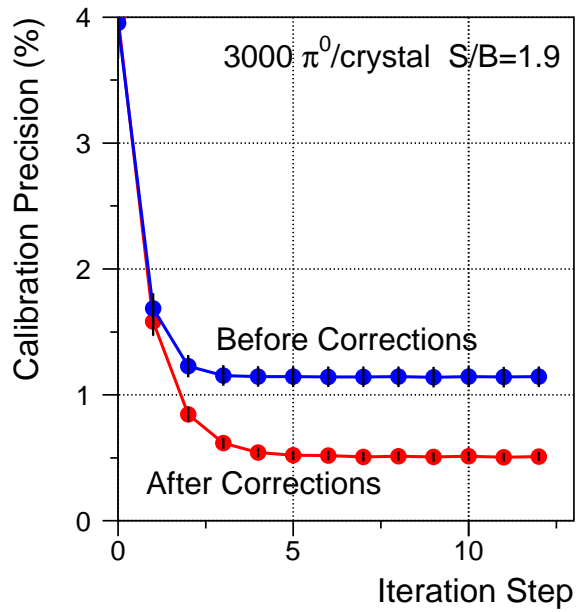


Figure 18: Improvement in the calibration accuracy after applying corrections for the selective readout and gaps between the ECAL supermodules/baskets.

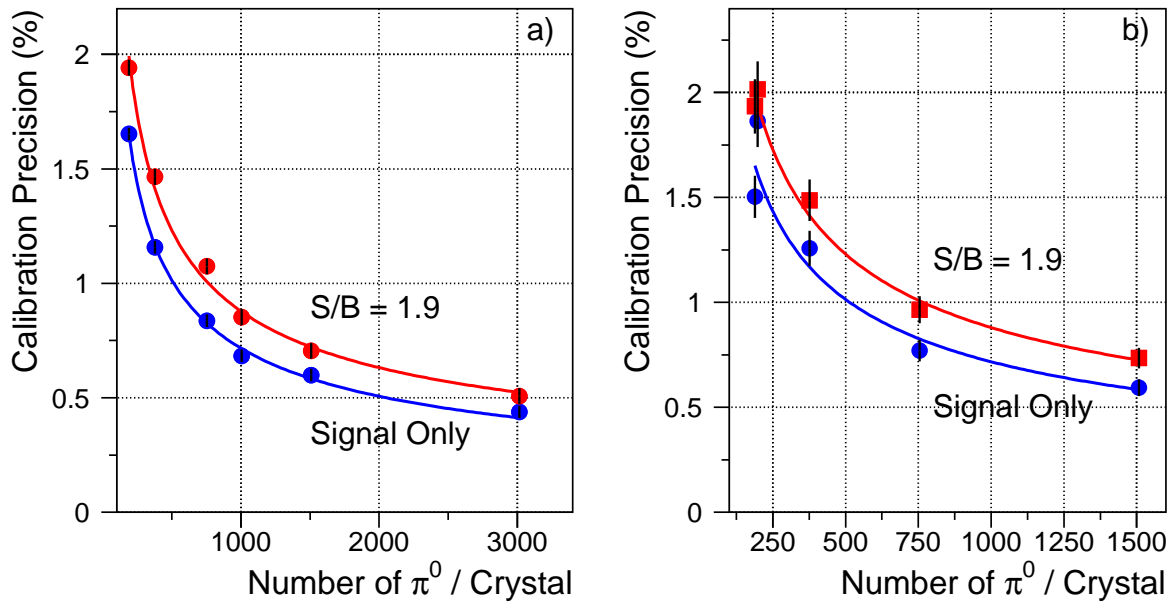


Figure 19: Calibration precision as a function of the number of signal π^0 's per crystal: a) before and b) after dividing the calibration sample into independent subsamples.

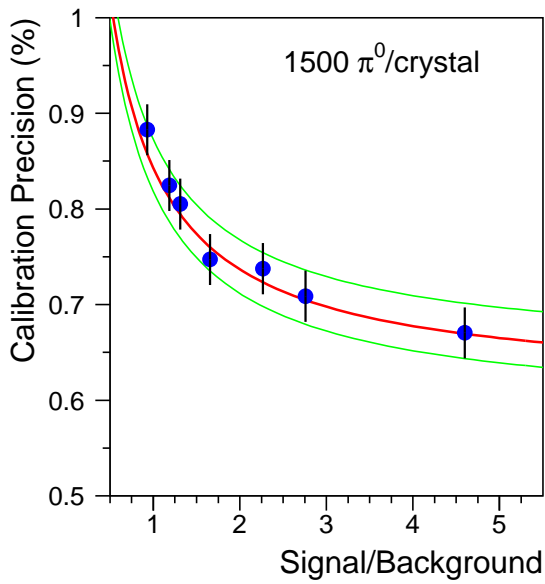


Figure 20: Calibration precision as a function of the S/B ratio. The curve corresponds to the function described in the text, and the green band represents the statistical uncertainty on function parameters.

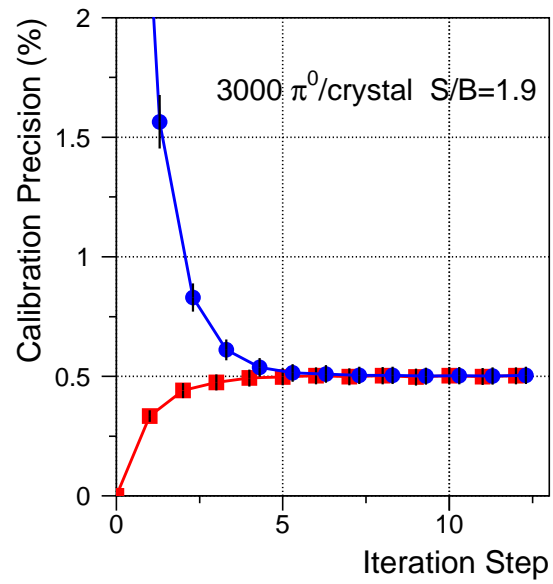


Figure 21: Comparison of the calibration precisions obtained with a 4% initial miscalibration and without any initial miscalibration.

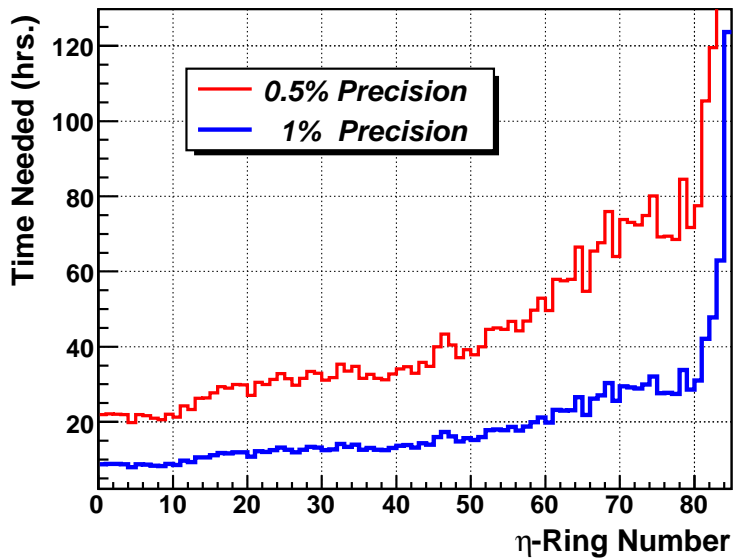


Figure 22: Time required to achieve calibration precisions of 1% and 0.5% for crystals in different η -rings.

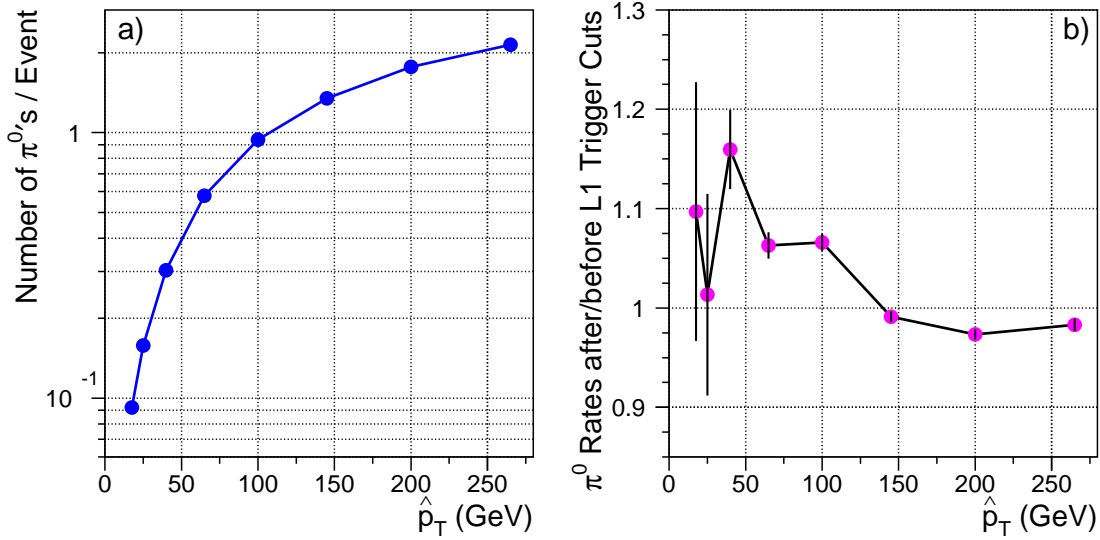


Figure 23: a) π^0 production rate at generator level as a function of \hat{p}_\perp , and b) the relative change in this rate observed after requiring the L1 trigger acceptance.

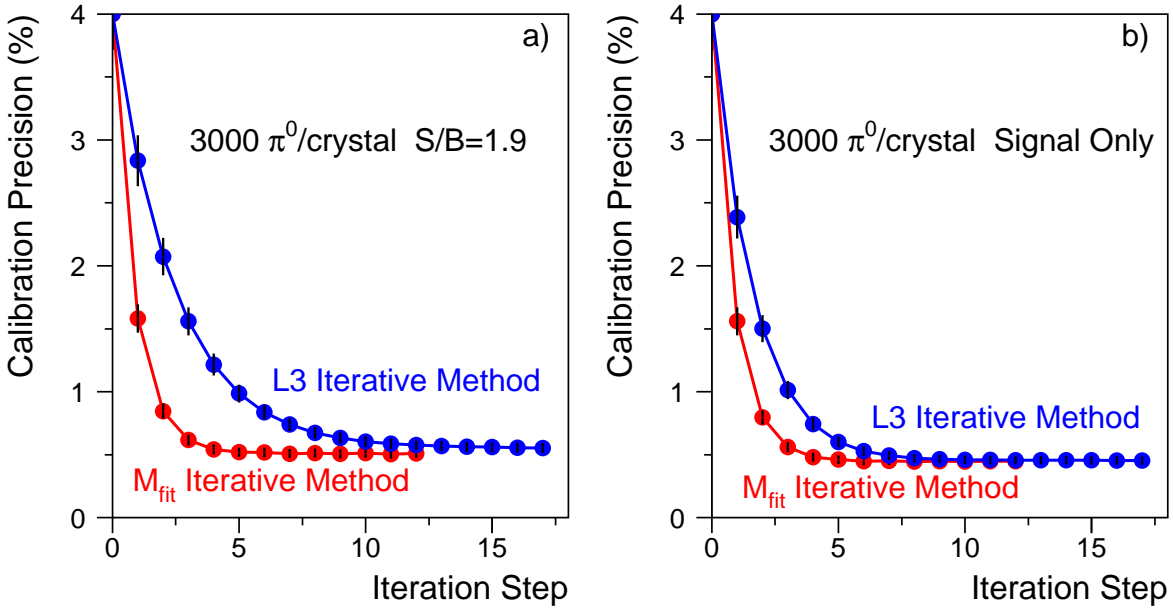


Figure 24: Comparisons between the L3 and M_{fit} fitting methods, showing the obtained calibration precisions as functions of the iteration step: a) for the case of $S/B = 1.9$ and b) for the signal-only sample.

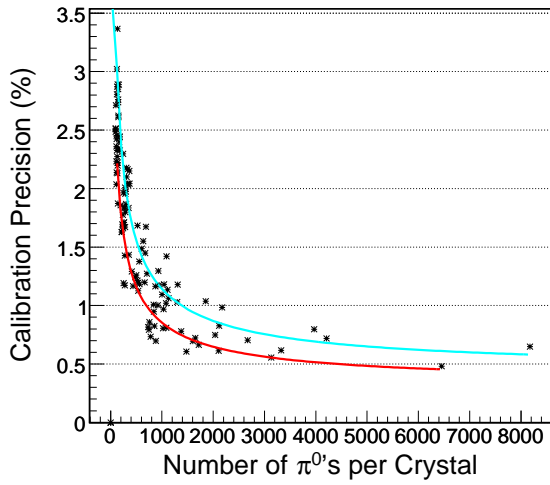


Figure 25: Calibration performance of the matrix inversion algorithm before (red) and after (cyan) excluding background events.

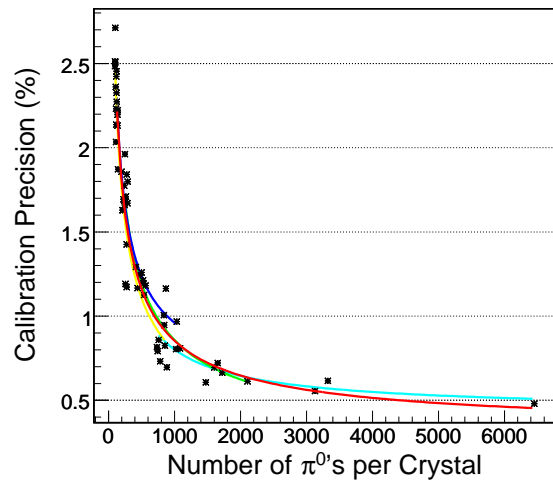


Figure 26: Calibration performance for different choices of folding (signal-only): 11×11 (yellow curve), 10×10 (blue), 7×7 (green), and 4×4 crystals (cyan). The red curve is a fit to all foldings.